

Tracheal and Central Bronchial Aerodynamics Using Virtual Bronchoscopy

Ronald M. Summers^{1*} and Juan R. Cebal²

¹Diagnostic Radiology Department, Warren Grant Magnuson Clinical Center
National Institutes of Health, Bethesda, MD 20892-1182

and

²School of Computational Sciences
George Mason University, Fairfax, VA 22030

ABSTRACT

Virtual bronchoscopy reconstructions of the airway noninvasively provide useful morphologic information of structural abnormalities such as stenoses and masses. In this paper, we show how virtual bronchoscopy can be used to perform aerodynamic calculations in anatomically realistic models. Pressure and flow patterns in a human airway were computed noninvasively. These showed decreased pressure and increased shear stress in the region of a stenosis.

Keywords: Bronchus; trachea; Wegener's granulomatosis; computational fluid dynamics; virtual bronchoscopy; visualization

1. INTRODUCTION

Virtual bronchoscopy is known to be useful for detecting airway stenoses due to inflammation, tumor, or post-operative change¹⁻⁶. Virtual bronchoscopy is a non-invasive technique done by taking helical CT scans of a patient's chest. These scans are then used to reconstruct endoluminal views of the airway which simulate what a pulmonologist would see during a conventional bronchoscopy.

A detailed description of the airflow is very complicated due to the extreme difficulty in the use of measurement techniques in human subjects⁷. Thus, there is a need to use both experimental and numerical models. The anatomy of the tracheobronchial tree is characterized by a three-dimensional, asymmetric branching pattern. Therefore, realistic models are preferred over idealized isolated airway bifurcation models. Airflow not only depends strongly on the geometry of the airways but also is intrinsically time-dependent. As a consequence the flow is extremely complex. This complexity makes it very difficult to obtain flow patterns and pressure drops simultaneously in experimental models. On the other hand, 3D numerical models allow the simultaneous estimation of velocity profiles, pressure drops and velocity gradients (shear stresses).

Virtual bronchoscopy reconstructions are ideally suited for determining aerodynamics of ventilation in the normal and diseased state. Using unstructured-grid computational fluid dynamics (CFD), we have measured air pressure and wall shear stress in the central airways of a patient with Wegener's granulomatosis and known airway disease.

2. METHODS

The subject was a 37-year old man with Wegener's granulomatosis, a necrotizing inflammatory disease that affects the airways⁸. The patient had a known stenosis in the bronchus intermedius confirmed bronchoscopically.

* Send correspondence to R.M.S.

E-mail: rms@nih.gov

Web site: <http://www.cc.nih.gov/drd/summers.html>

Thoracic CT scans were done using a single-slice helical CT scanner (SS-CT) (General Electric HiSpeed Advantage). Scanning was done from the level of the vocal cords through the costophrenic sulci using 3 mm collimation, helical pitch 2 (6 mm table motion per rotation), 140 kVp, 160 mAs, 1 sec tube rotation, overlapping reconstructions with a section interval of 1 mm, and an effective z-axis resolution of approximately 4.6 mm. Scanning was done in two or three breathholds. A bone reconstruction algorithm was used.

A three-dimensional virtual bronchoscopy model of the patient's central airways were produced using previously reported techniques⁶. Region growing was done to identify voxels within the airway lumen. A marching cubes algorithm generated the isosurface as a triangle mesh. The triangle mesh was smoothed to reduce effects of spiral artifact and noise. Triangle meshes were stored as Open Inventor scene graphs. Processing was performed using custom C++ code running on an SGI Indigo2 with Maximum Impact graphics. The virtual bronchoscopy reconstruction is shown in Figure 1. The known stenosis in the bronchus intermedius is visible (Figure 1a,b).

A finite element grid was generated from the virtual bronchoscopy reconstructions. Prior to the grid generation, a pre-processing algorithm was applied to the surface model⁹. This algorithm first identifies and removes *unused points*, i.e. not connected to any triangle, and *duplicated points*, i.e. points closer than a certain tolerance (e.g. 10^{-8}). The surface is then *smoothed* using a non-shrinking smoothing technique in order to eliminate small-scale noise in the surface geometry. The surface triangulation is then optimized. An *edge-collapsing* algorithm is then used to delete very small elements or elements with large aspect ratios. Finally, a *diagonal-swapping* procedure is applied to minimize the maximum angle between adjacent triangles. Edge-collapses and diagonal-swaps are prevented if the new configuration changes substantially the normals of the surrounding elements. The result of this pre-processing step is a smooth surface triangulation with no holes, gaps, self-intersections or overlapping elements (figure 1c). The surface model was then *cut* in order to obtain planar surfaces at the locations where in/outflow boundary conditions are to be imposed for the flow equations (figure 1d).

This geometrical model was then used as a support surface to define the 3D computational domain to be gridded. A new surface triangulation was generated on top of the support surface with the desired element size distribution using an advancing front technique and topological constraints to avoid intersections between close branches¹⁰. A background grid was used to specify a uniform element size distribution corresponding to roughly ten elements across the smallest outflow boundary. Background sources were used to increase the grid resolution in the region of the stenosis. Starting from this new triangulation, the space inside the geometrical model was then filled up with tetrahedral elements using an advancing front algorithm¹¹. The generated volumetric mesh contained roughly a million elements and 185K nodes (figure 1e).

Two CFD simulations were carried out: a steady calculation during inspiration and an unsteady calculation that comprises both inspiration and expiration. The incompressible Navier-Stokes equations were advanced in time using a stabilized fractional step method¹². Spatial discretization was performed using finite elements (linear tetrahedra). A Generalized Minimal Residual (GMRES) method was used to solve the discretized momentum equation and a conjugate gradient technique for the Poisson pressure equation. For the steady state calculation, an explicit time integration of the advective terms and an implicit integration of the pressure and viscous terms were used. Although very accurate, the stability condition of the explicit time integration imposes limits in the maximum time-step size that can be used, rendering the algorithm impractical for unsteady calculations. Therefore, a fully implicit time integration scheme was used for the transient computation. This allowed the selection of a time-step much larger than the explicit time-step. One complete breathing cycle (inspiration and expiration) was subdivided into 64 time-steps. Even though the internal iterations for the GMRES and conjugate gradient solvers also increase substantially, the overall computation time is drastically reduced.

At the inflow boundary, a fully developed velocity profile was imposed as boundary condition. For the unsteady calculation, a time dependent velocity profile was specified from a time-dependent volume flow curve using the Womersley solution. The flow curve was derived from a time dependent volume curve taken from the literature¹³. The Reynolds number, calculated using the radius of the inflow boundary, ranged from 0 to about 1500. For the steady state run, a Poiseuille (parabolic) velocity profile was specified corresponding to the average volume flow during inspiration. It was assumed that all the outlets discharge to the same fixed pressure. Thus, a traction-free boundary condition with $p=0$ was imposed at all the exits. This assumption is reasonable since most of the pressure drops occurs between the outlets of our model and the lungs, i.e. there is only a small pressure drop between the trachea and the outlets of our model. Of course, the denomination of "outlets" should not be taken literally since during expiration in the unsteady runs the flow reverses and they become inlets. The walls of the airways were assumed rigid and no-slip ($\mathbf{v} \cdot \mathbf{n} = 0$) boundary conditions were imposed.

An integrated set of software tools was used to conduct the numerical simulations. The CFD calculations were performed using FEFLO¹⁴, an in house flow solver, running in parallel mode on a Silicon Graphics Origin2000 with 16 R10K processors. In house software was also used for pre-processing (ZMED)¹⁵, grid generation (GEN3D)¹⁶ and visualization (ZFEM)¹⁷ running on a Silicon Graphics Octane workstation.

3. RESULTS

In the case of the steady airflow during inspiration, we found an increased pressure drop at the site of the stenosis (figures 2a and 2b). This is due to the flow acceleration that takes place as a consequence of the narrowing of the airway lumen at the stenosis. Higher pressure at the bifurcation right before the stenosis was also found, indicating the presence of a stagnation region in the inner wall of the bifurcation (figure 2b). A flow visualization using streamlines colored according to the flow velocity magnitude (figures 2c and 2d) revealed a complicated flow pattern with recirculation regions downstream of the stenosis. The flow division pattern was visualized by plotting streamlines going into different airway branches with different colors (figure 2e).

The results from the unsteady aerodynamics computation show a more complicated flow pattern, especially during the inspiratory phase. A visualization of the instantaneous pressure distribution shows a reversal of the pressure gradient from inspiration to expiration (figure 3a and b). A visualization of the wall shear stress distribution (figures 3c and 3d) shows that higher stresses tend to concentrate in regions of high curvature, indicating the presence of strong secondary flows. An overall change in the shear stress distribution from inspiration to expiration, caused by a marked difference in the secondary flows is also evident.

A visualization of the instantaneous pressure distribution in the region of the stenosis (figures 4a, 4b and 4c) reveals an increased pressure drop at the site of the stenosis during inspiration, consistent with the steady results. However, this effect is more evident only at certain instants near the peak of the flow curve. Shear stress maps (figures 4d, 4e and 4f) show an increased wall shear stress at the site of the stenosis as well as a complicated, time-varying flow field with regions of separation and recirculation. During the expiratory phase, the flow pattern is less complicated, the pressure drop at the stenosis is less marked, and flow recirculation zones are not evident distal from the stenosis.

Visualizations of the transient velocity field in the region of the stenosis (figure 5) show complex time-dependent flow recirculation and separated regions downstream of the stenosis during inspiration. An increased flow velocity at the stenosis (jet) during inspiration can also be seen (figures 5a and 5b). However, the location of the maximum velocity at a given cross section changes in time. Velocity profiles are skewed and show flow recirculation and secondary flows (figures 5d and 5e) during inspiration, but a much simpler flow pattern with no recirculation during expiration (figure 5c and 5f).

4. DISCUSSION

Airway stenosis is a significant cause of morbidity and mortality in patients with cancer, pneumonia, and collagen-vascular diseases affecting the chest. Primary or metastatic neoplasm which compresses or invades an airway often causes collapse of the lung segment fed by the affected bronchus. Infection and collagen-vascular diseases can cause inflammation and the endobronchial healing response can cause fibrosis or web formation which can narrow or occlude an airway. Treatment is centered on the underlying cause and can include radiation treatment, chemotherapy, antibiotics, or surgery. Endoscopic interventional procedures to treat stenosis include balloon dilatation and stent placement.

Early airway flow models consisted in idealized symmetrical planar bifurcations or series of bifurcations in which steady axial and secondary flow were measured experimentally¹⁸. Steady and unsteady flow results were later obtained in more realistic airway models¹⁹⁻²². More recently, simultaneous measurements of flow patterns and pressure drops were performed in realistic 3D hollow lung cast models, both experimentally and numerically²³.

Anatomical models reconstructed from CT images include corrugations in the first airway generation due to the presence of cartilage rings. These small-scale features affect the local flow characteristics and consequently the determination of pressure drops and shear stress distributions.

With existing helical CT scanners, there is a trade-off between longitudinal resolution and anatomical extent of coverage. Artifactual discontinuities can occur in the reconstructed anatomical model when scanning must pause so the patient can breathe. One such artifact, although relatively minor, occurred in our model and can be seen in the distal trachea (Figure 1b, very top of image). The latest generation multi-slice helical CT (MS-CT) scanners are fast enough to scan the entire thorax in a single breathhold at high resolution and should be able to eliminate such artifacts. Another reconstruction artifact, called “spiral artifact”, will also be reduced with MS-CT²⁴.

Pressure drop calculations based on unidirectional flow models (1D electric network analogs) are limited by the assumption of a fully developed, uniform velocity profile at every location along the airway tree. As shown by our computations this never happens, even under steady flow conditions.

Our model assumed rigid airway walls. This approximation, which is common to most experimental and numerical models, is acceptable in normal quiet breathing since variations of the length and diameter of the airways remain moderate. In rapid and deep breathing, the flow may change significantly and this assumption may not be appropriate.

The tracheobronchial tree consists in a rapidly branching system with a considerable increase in total cross-sectional area of the parallel pathways in order to give rise to a large alveolar surface area. In normal conditions, the airway resistance is small in order to minimize as much as possible the inspiratory effort. These two facts imply that most of the pressure drop occurs beyond the first or second airway generation. This justifies the assumption of equal pressure at all the outlets of our model. A more refined model that relates the pressure at a given outlet to its area may be derived from the assumption that beyond this point the airway bifurcates a large number of times until it reaches the alveoli where the pressure is known.

In conclusion, aerodynamic computations can be performed from virtual bronchoscopy reconstructions. Pending validation by using flow measurements on physical models, the significance of these capabilities is that they allow physicians to noninvasively assess the pathophysiologic significance of airway stenoses and potentially predict when intervention may be required before stenoses become symptomatic.

ACKNOWLEDGMENTS

We thank Dr. Peter Yim for review of the manuscript and Dr. Michael Sneller for patient referral.

REFERENCES

1. D. J. Vining, K. Liu, R. H. Choplin and E. F. Haponik, "Virtual bronchoscopy. Relationships of virtual reality endobronchial simulations to actual bronchoscopic findings," *Chest* **109**, pp. 549-53, 1996.
2. H. U. Kauczor, B. Wolcke, B. Fischer, P. Mildenerberger, J. Lorenz and M. Thelen, "Three-dimensional helical CT of the tracheobronchial tree: evaluation of imaging protocols and assessment of suspected stenoses with bronchoscopic correlation," *Am J Roentgenol* **167**, pp. 419-24, 1996.
3. G. R. Ferretti, J. Knoplioch, I. Bricault, C. Brambilla and M. Coulomb, "Central airway stenoses: preliminary results of spiral-CT-generated virtual bronchoscopy simulations in 29 patients," *Eur Radiol* **7**, pp. 854-9, 1997.
4. W. E. Higgins, K. Ramaswamy, R. D. Swift, G. McLennan and E. A. Hoffman, "Virtual bronchoscopy for three-dimensional pulmonary image assessment: state of the art and future needs," *Radiographics* **18**, pp. 761-78, 1998.
5. H. P. McAdams, S. M. Palmer, J. J. Erasmus, E. F. Patz, J. E. Connolly, P. C. Goodman, D. M. Delong and V. F. Tapson, "Bronchial anastomotic complications in lung transplant recipients: virtual bronchoscopy for noninvasive assessment," *Radiology* **209**, pp. 689-95, 1998.
6. R. M. Summers, D. H. Feng, S. M. Holland, M. C. Sneller and J. H. Shelhamer, "Virtual bronchoscopy: segmentation method for real-time display," *Radiology* **200**, pp. 857-62, 1996.
7. D. Isabey, R. Fodil and B. Louis, *Steady flow models of upper airways and lower airways*, Belgium, 1998.
8. M. C. Sneller, "Wegener's granulomatosis [clinical conference] [see comments]," *JAMA* **273**, pp. 1288-91, 1995.
9. J. R. Cezbal and R. Lohner, "From medical images to anatomically accurate finite element grids," *International Journal For Numerical Methods in Engineering* pp. in press, 2000.
10. R. Lohner, "Regridding surface triangulations," *Journal of Computational Physics* **126**, pp. 1-10, 1996.
11. R. Lohner, "Automatic unstructured grid generators," *Finite Elements in Analysis and Design* **25**, pp. 111-134, 1997.
12. J. R. Cezbal, R. Lohner and J. E. Burgess, "Computer simulation of cerebral artery clipping: Relevance to aneurysm neuro-surgery planning," *Proc. of ECCOMAS 2000* pp. in press, Barcelona, Spain, 2000.
13. W. F. Ganong, *Review of medical physiology*, 10th edition ed., Lange Medical Publications, Los Altos, CA, 1981.
14. R. Lohner, C. Yang, J. R. Cezbal, O. Soto, C. Camelli, J. Baum, H. Luo, E. Mestreau and D. Sharov "Advances in FEFLO," AIAA-01-0592, January, 2001.
15. J. R. Cezbal and R. Lohner, "From Medical Images To CFD Meshes," *Proc. 8th International Meshing Roundtable* pp. , South Lake Tahoe, California, 1999.
16. R. Lohner and J. R. Cezbal, "Parallel Advancing Front Grid Generation," *Proc. 8th International Meshing Roundtable* pp. , South Lake Tahoe, California, 1999.
17. J. R. Cezbal and R. Lohner "Interactive On-Line Visualization and Collaboration for Parallel Unstructured Multidisciplinary Applications," AIAA-98-0077, January, 1998.
18. T. J. Pedley, R. C. Shroter and M. F. Sudlow In *Bioengineering Aspects of the Lung*; J. West, Ed.; Marcel Dekker Inc.: New York, 1977; pp 163-265.
19. H. K. Chang In *Respiratory Physiology an Analytical Approach*; H. Chang, Ed.; Marcel Dekker Inc.: New York, 1989; pp 57-138.
20. D. L. Jan, A. H. Shapiro and R. D. Kamm, "Some Features of Oscillatory Flow in a Model Bifurcation," *Journal of Applied Physiology* **67**, pp. 147-159, 1989.
21. D. L. Jan, "Correction," *Journal of Applied Physiology* **67**, pp. U917-U917, 1989.
22. A. Tsuda, R. Kamm and J. J. Fredberg, "Periodic-Flow At Airway Bifurcations .2. Flow Partitioning," *Journal of Applied Physiology* **69**, pp. 553-561, 1990.
23. F. Wilquem and G. Degrez, "Numerical modeling of steady inspiratory airflow through a three-generation model of the human central airways," *Journal of Biomechanical Engineering-Transactions of the Asme* **119**, pp. 59-65, 1997.
24. D. Fleischmann, G. D. Rubin, D. S. Paik, S. Y. Yen, P. R. Hilfiker, C. F. Beaulieu and S. Napel, "Stair-step artifacts with single versus multiple detector-row helical CT," *Radiology* **216**, pp. 185-96, 2000.

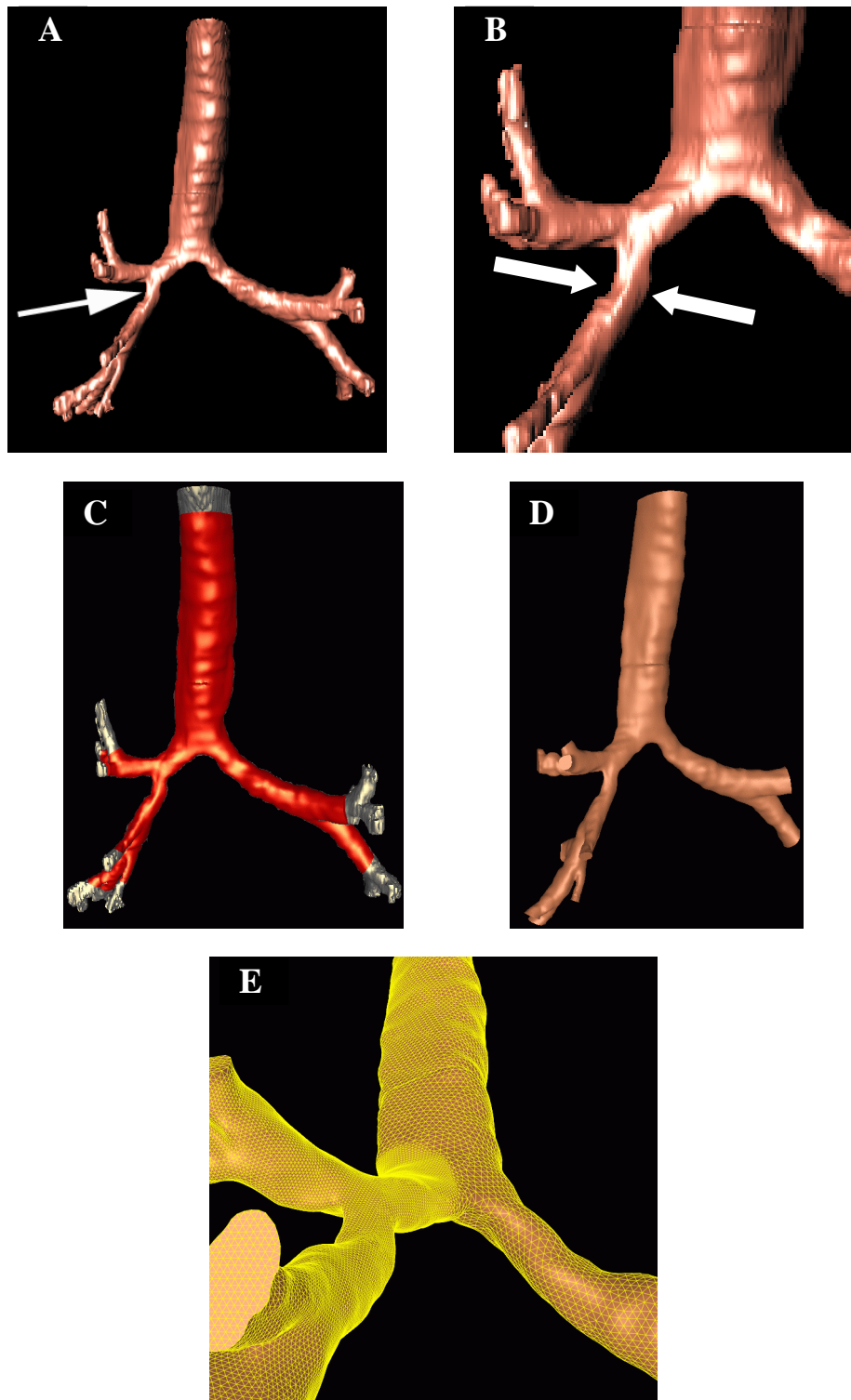


Figure 1. Preparing the geometry. (A,B) Original airway geometry (A, anteroposterior view; B, magnified view showing carina and right lung airways). Bronchus intermedius stenosis is shown (arrows). (C,D) The first step was to cut off the distal bronchi. (E) Next, a finite element mesh was fit to the airway.

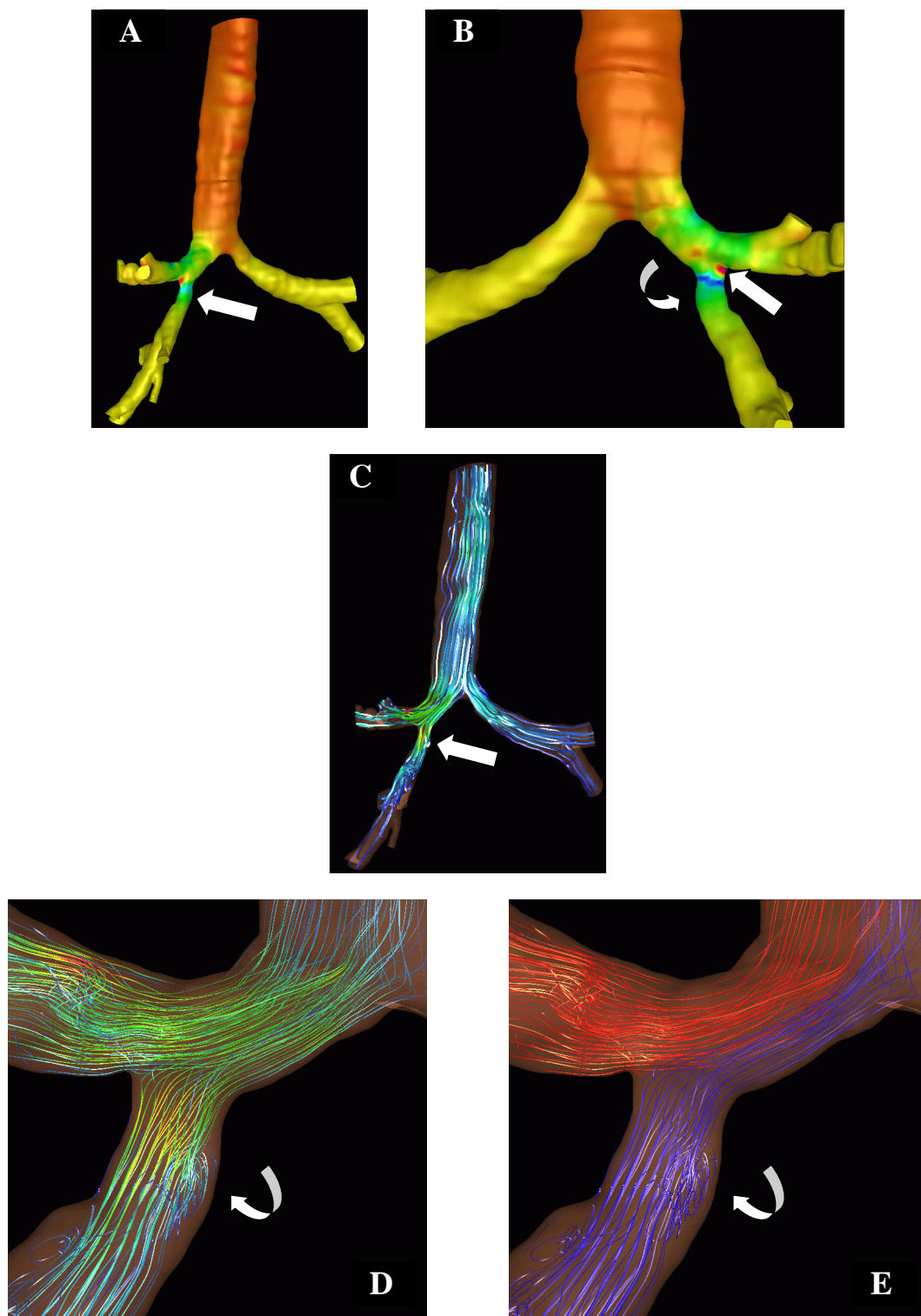


Figure 2. Aerodynamic computations. Visualizations from a computational fluid dynamics simulation are shown. (A, B) Pressure maps show decreased pressure in the region of the stenosis (arrows). Note focus of high pressure at the bifurcation (straight arrow in B). (C, D, E) Streamlines show flow patterns through stenosis (straight arrow in C). Note recirculation pattern along medial wall of stenosis (curved arrows).

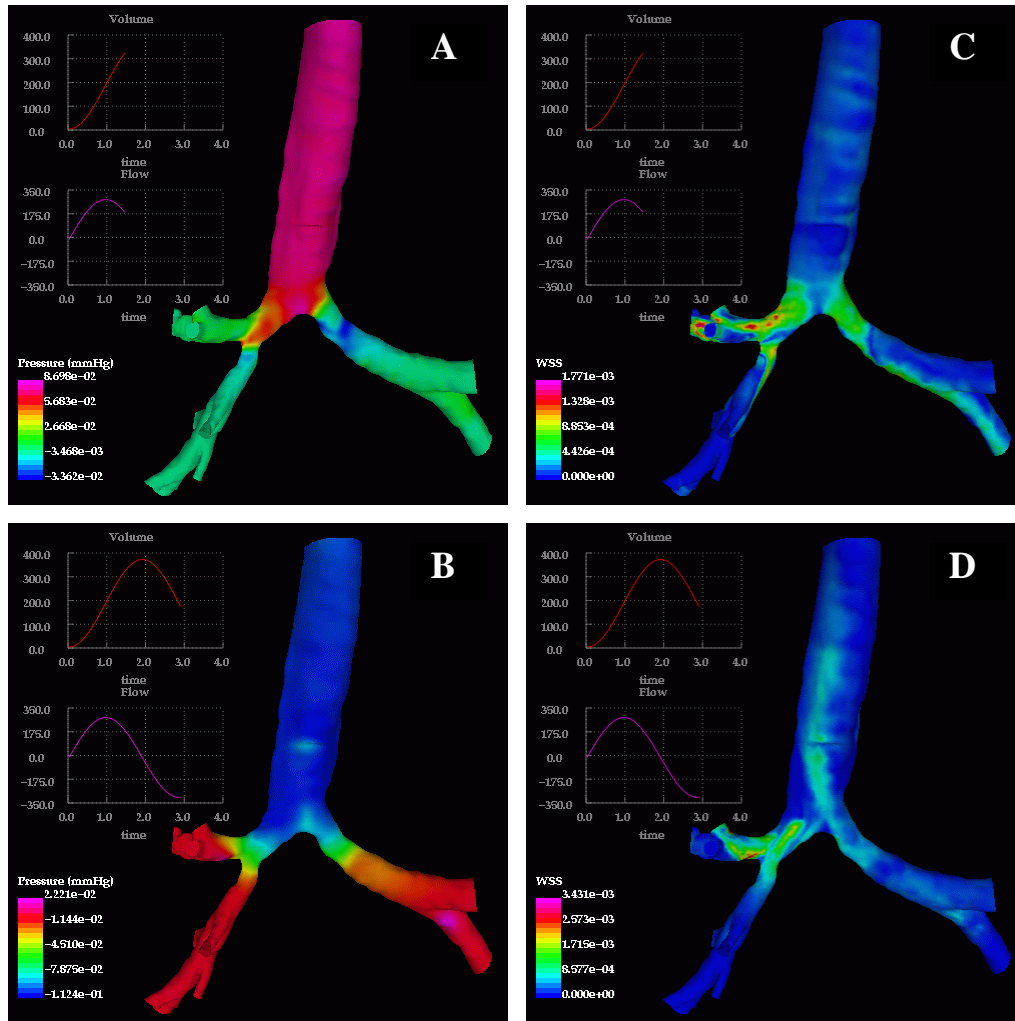


Figure 3. Unsteady aerodynamics simulation. Instantaneous pressure distributions during inspiration (A) and expiration (B) are shown. At the same instants of time, wall shear stress distributions are also shown (C,D). Note the reversal of the pressure gradient from inspiration to expiration, the concentration of high shear stress in regions of high curvature implying strong secondary flows, and the change in the shear stress distribution from inspiration to expiration.

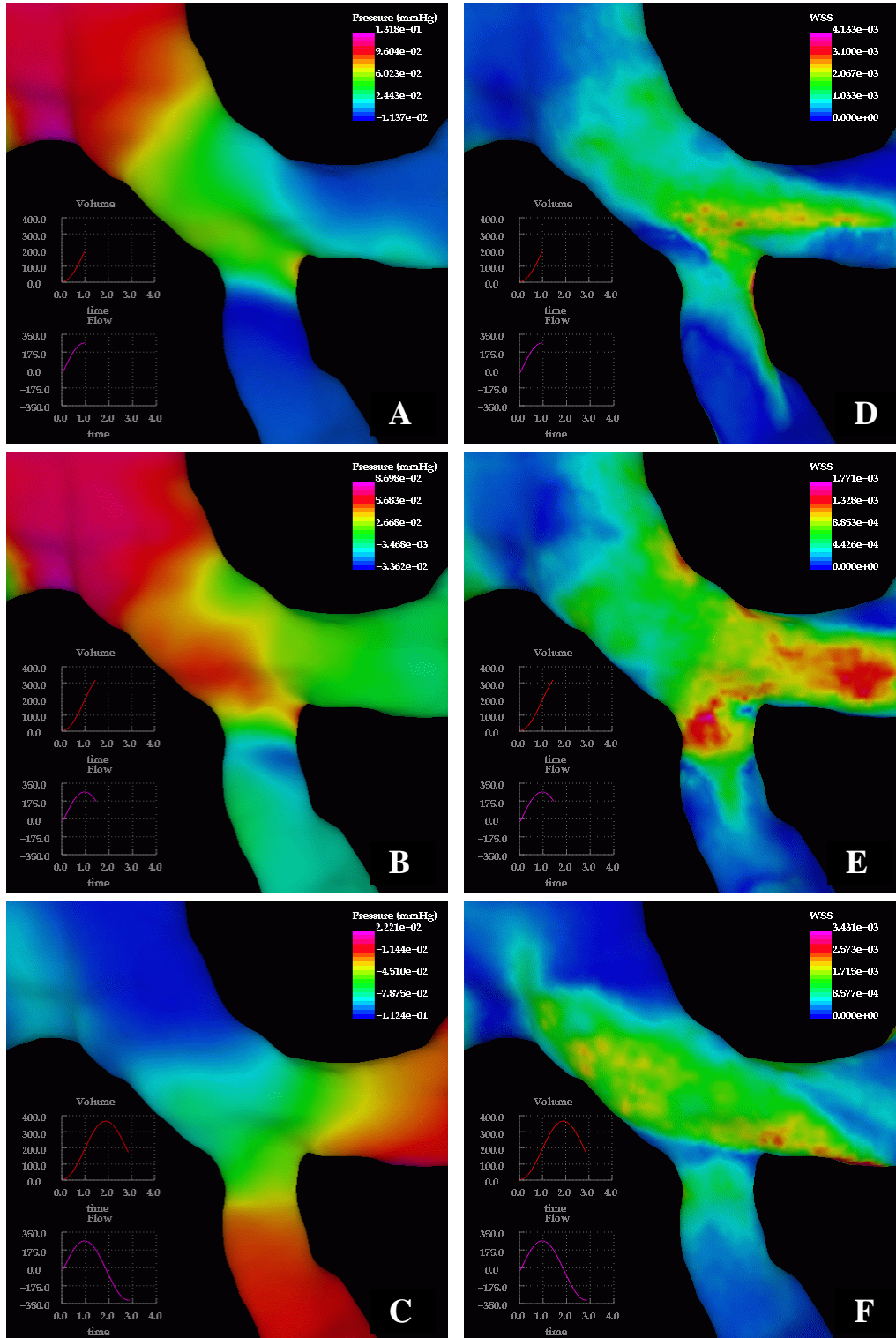


Figure 4. Visualization of unsteady aerodynamics calculation in the site of stenosis. Pressure distributions at different instants during inspiration (A,B) and expiration (C) are shown. Wall shear stress maps at the same instants of time are also shown (D,E,F). Note the increased pressure drop and shear stress at the stenosis during inspiration (B,E) and regions of flow separation (blue lines in shear stress maps). Compared to Figures 1-3, the airway has been flipped left-to-right for display purposes.

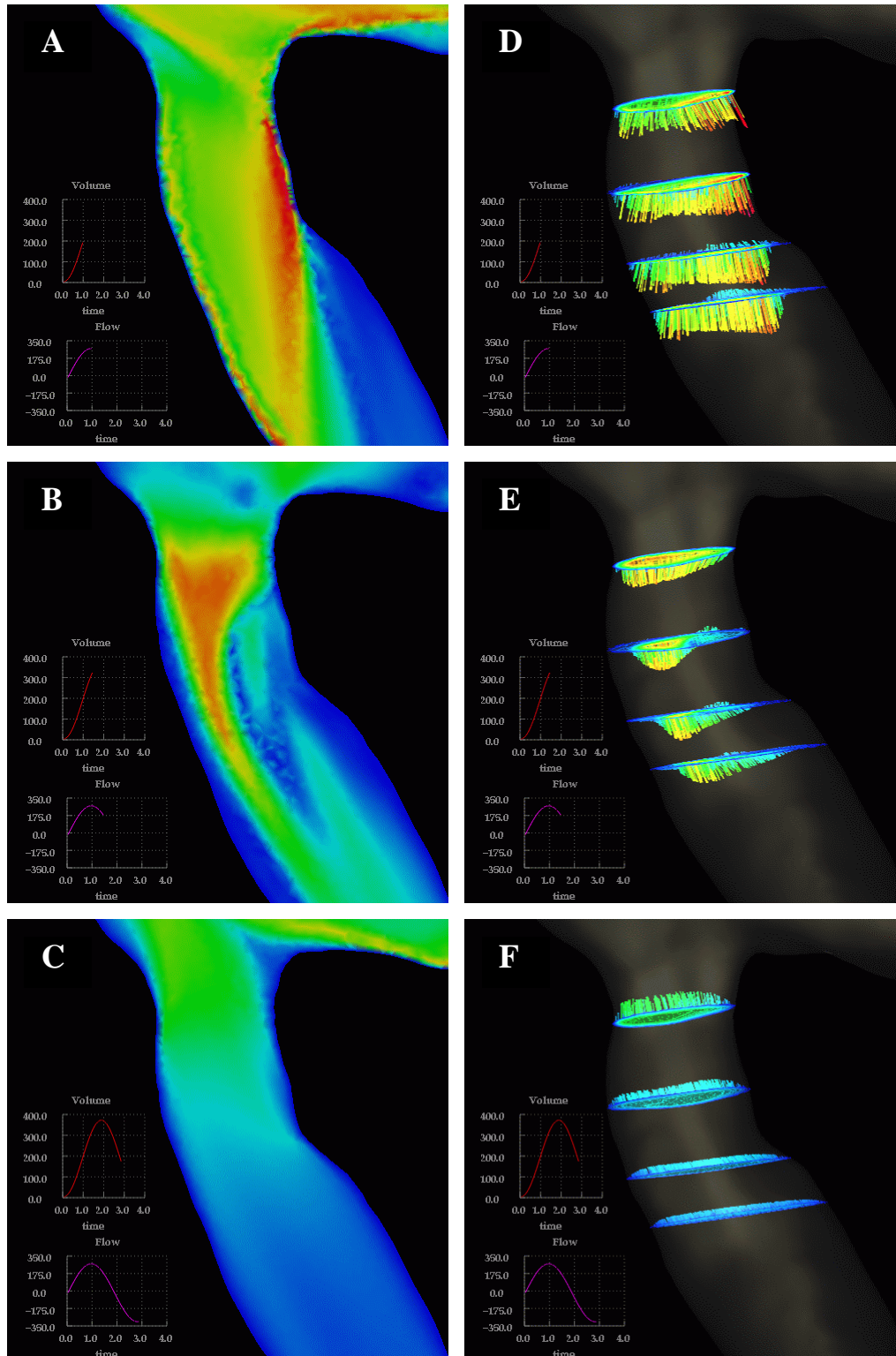


Figure 5. Unsteady aerodynamics flow visualizations in the region of the stenosis. A cut-plane parallel to the axis of the airway is used to display the flow velocity magnitude at different instants during inspiration (A,B) and expiration (C). Velocity profiles are shown on four cut-planes normal to the axis of the airways at the same instants of time (D,E,F). Note the complicated flow recirculation regions distal of the stenosis and skewed velocity profiles during inspiration and much simpler flow pattern during expiration. Compared to Figures 1-3, the airway has been flipped left-to-right for display purposes.